



UNIVERSITY OF LEEDS

This is a repository copy of *CFD predictions of wake-stabilised jet flames in a cross-flow*.

White Rose Research Online URL for this paper:

<http://eprints.whiterose.ac.uk/79573/>

Version: Accepted Version

---

**Article:**

Lawal, MS, Fairweather, M, Ingham, DB et al. (4 more authors) (2013) CFD predictions of wake-stabilised jet flames in a cross-flow. *Energy*, 53. 259 - 269. ISSN 0360-5442

<https://doi.org/10.1016/j.energy.2013.02.020>

---

**Reuse**

Unless indicated otherwise, fulltext items are protected by copyright with all rights reserved. The copyright exception in section 29 of the Copyright, Designs and Patents Act 1988 allows the making of a single copy solely for the purpose of non-commercial research or private study within the limits of fair dealing. The publisher or other rights-holder may allow further reproduction and re-use of this version - refer to the White Rose Research Online record for this item. Where records identify the publisher as the copyright holder, users can verify any specific terms of use on the publisher's website.

**Takedown**

If you consider content in White Rose Research Online to be in breach of UK law, please notify us by emailing [eprints@whiterose.ac.uk](mailto:eprints@whiterose.ac.uk) including the URL of the record and the reason for the withdrawal request.



[eprints@whiterose.ac.uk](mailto:eprints@whiterose.ac.uk)  
<https://eprints.whiterose.ac.uk/>

# CFD predictions of wake-stabilised jet flames in a cross-flow

Mohammed S. Lawal<sup>a</sup>, Michael Fairweather<sup>a</sup>, Peter Gogolek<sup>b</sup>, Derek B. Ingham<sup>a</sup>, Lin Ma<sup>a†</sup>, Mohamed Pourkashanian<sup>a</sup> and Alan Williams<sup>a</sup>

<sup>a</sup> *CFD Centre, Energy Technology and Innovation Initiative, University of Leeds, Leeds LS2 9JT, UK*

<sup>b</sup> *CANMET Energy and Technology Centre Flare Test Facility, Natural Resources Canada, 1 Haanel Drive, Ottawa, Ontario K1A 1M1, Canada*

<sup>†</sup> *Corresponding author; T: +44(0)1133438954, F: +44(0)1132467310, E: l.ma@leeds.ac.uk*

## Abstract

This study describes an investigation into predicting the major flow properties in wake-stabilised jet flames in a cross flow of air using first- and second-order turbulence models, applied within a Reynolds-averaged Navier-Stokes (RANS) modelling framework. Standard and re-normalisation group (RNG) versions of the  $k-\varepsilon$  turbulence model were employed at the first-order level and the results compared with a second-moment closure, or Reynolds stress model (RSM). The combustion process was modelled using the laminar flamelet approach together with a thermal radiation model using the discrete ordinate method. The ability of the various turbulence models to reproduce experimentally established flame appearance, profiles of velocity and turbulence intensity, as well as the combustion efficiency of such flames is reported. The results show that all the turbulence models predict similar velocity profiles over the majority of the flow domain considered, except in the wake region, where the predictions of the RSM and RNG  $k-\varepsilon$  models are in closer agreement with experimental data. In contrast, the standard  $k-\varepsilon$  model over-predicts the peak turbulence intensity. Also, it is found that the RSM provides superior predictions of the planar recirculation and flame zones attached to the release pipe in the wake region.

**Keywords:** Turbulence modelling, non-premixed flames, cross-flow, wake effects

## Nomenclature

$d$	Pipe diameter (m)
$g$	Acceleration due to gravity ( $\text{m/s}^2$ )
$k$	Turbulence kinetic energy ( $\text{m}^2/\text{s}^2$ )
$L$	Path length (m)
$p$	Pressure ( $\text{N/m}^2$ )
$R$	Jet to cross-flow momentum flux ratio (1)
$Re_w$	Reynolds number based on cross-flow velocity (1)
$S$	Strain rate (1/s)
$t$	Time (s)
$T$	Temperature (K)
$u$	Velocity (m/s)
$x$	x-component of the Cartesian coordinate system (m)
$y$	y-component of the Cartesian coordinate system (m)
$z$	z-component of the Cartesian coordinate system (m)
$\varepsilon$	Rate of dissipation of turbulence kinetic energy ( $\text{m}^2/\text{s}^3$ )
$\varepsilon_0$	Emissivity (1)
$\eta_t$	Combustion efficiency (1)
$\kappa$	Absorption coefficient (1)
$\mu_{eff}$	Effective turbulent viscosity (Pa s)
$\mu_t$	Turbulent eddy viscosity (Pa s)
$\nu$	Kinematic viscosity ( $\text{m}^2/\text{s}$ )
$\rho$	Density ( $\text{kg/m}^3$ )
$\chi$	Scalar (mixture fraction) dissipation rate (1/s)

## Subscript

$j$	Jet
$cf$	Cross flow

**Acronym**

CETC	Canada Energy Technology Centre
CVP	Counter-rotating vortex pair
EVM	Eddy-viscosity turbulence model
NEVM	Non-linear eddy-viscosity turbulence model
RANS	Reynolds-averaged Navier-Stokes
RNG	Renormalisation Group
RSM	Reynolds stress model
UoA	University of Alberta
JFICF	Jet flame in cross-flow
WSGGM	Weighted-sum-of-grey gases method

## 1. Introduction

A large quantity of oil field associated gas, and waste hydrocarbons from the process industry, is flared globally each year. With the predicted increase in oil production in the next decades, a significant increase in flaring is expected [1,2]. However, flare operations can result in the formation of pollutants such as unburned hydrocarbons, CO, NO<sub>x</sub> and noise and the effect of a cross-flow of wind can be significant. In order to minimise these effects, a detailed understanding of the flow features and structures of these non-premixed jet flames in a cross-flow (JFICF) is necessary. Depending on the value of the jet-to-cross-flow momentum flux ratio,  $R = \rho_j u_j^2 / \rho_{cf} u_{cf}^2$ , where  $\rho_j$ ,  $\rho_{cf}$  and  $u_j$ ,  $u_{cf}$  are the density and velocity of the fuel jet and the cross-flow, respectively, the flow features that arise in the JFICF have an important influence on the flame's combustion characteristics.

For flares operating at low values of  $R$ , typically  $R \leq 1.0$ , the flame is either seated on the flare stack or stabilised in its wake [3]. The latter case is also known as a wake-stabilised flare which belongs to a flow regime where the flame is severely bent-over by the cross-flow and has high turbulence intensities in the near-field [4]. This category of flare is commonly found in offshore crude oil production facilities.

The three main flow features in the wake-stabilised flare include: a counter-rotating vortex pair (CVP) [5], coherent structures around the upper surface of the jet [3] and the planar recirculation zone in the wake of the stack [6]. The latter zone is part of the low-pressure region where a secondary flame is attached to the release pipe, as shown in Fig. 1, and the vortex dynamics and mixing in this region have an influence on the efficiency characteristics of the flame, particularly under high  $u_{cf}$  [7]. In wake-stabilised flares, therefore, interactions between the jet, the cross-flow and the release pipe generate complex turbulent mixing that dominates the flow field. Further, in non-premixed flames, turbulence has a significant effect on the concentration of chemical species produced [8].

Extensive laboratory-scale experimental studies of the low momentum JFICF as a model of wake-stabilised flares have been reported although mainly using propane as a fuel. These include measurements of profiles of temperature and major chemical species in laboratory-scale flames [6,9]. The velocity, vorticity field and turbulence intensity in the near-wake region, as well as the efficiency characteristics of such flames, have also been reported [10-12]. However, similar experimental measurements for industrial-scale methane or natural gas flares are not available.

Few studies have been made of numerical predictions of wake-stabilised flares. A massively parallel large eddy simulation (LES) has been used to investigate the impact of H<sub>2</sub>S on the combustion efficiency of such flames or indeed any flare [13]. However, the high computational cost of performing LES of flares limits its wide spread application. Consequently, most of the previous numerical studies of flares have employed RANS-based approaches to predicting the turbulent flow field. Previous attempts to predict the flame temperature in the far-field and planar flame zone in the wake of the release pipe using the standard  $k$ - $\epsilon$  turbulence model have been less than successful for both methane [14] and propane flares [15], and this was attributed to the inadequacy of the eddy-viscosity turbulence models (EVM) employed in these studies. To overcome these limitations within the RANS modelling framework, the authors suggest the use of second-moment turbulence closures, namely Reynolds stress models (RSM).

One of the major problems of the eddy-viscosity based  $k$ - $\epsilon$  turbulence models is their assumption of isotropic turbulent viscosity and this results in an overestimation of the Reynolds stress, which prevents the development of recirculating flow, and covering up the important directionally dependent nature of the Reynolds stress that may exist in the fluid flows. The RSM, on the other hand, solves for the six independent components of the Reynolds stress tensor separately and it is a second-order closure model. This can substantially improve the accuracy of the prediction of the flows with a high stretched and/or recirculating flow region, such as those occur in the coherent structures and the recirculation zone in the wake of the stack of the flare investigated in this paper. However, the extra costs that need to be paid of employing the RSM is the additional computational efforts for solving the additional partial differential equations for each direction and the difficulty in achieving convergence that often encounters.

Despite its potential to provide more accurate predictions of complex flow physics, the application of RSM in predicting the JFICF has not been investigated. Therefore this paper aims to contribute to the understanding of the ability of RSM to reproduce the important flow features in the wake-stabilised JFICF. To facilitate comparisons, in addition to the RSM two other turbulence models are investigated; these being the standard  $k$ - $\epsilon$  model [16] and the renormalization group (RNG) theory  $k$ - $\epsilon$  variant [17]. Here the ability of all these models to predict the flame appearance, profiles of its velocity and turbulence fields, and the flame's efficiency characteristics are investigated. This aspect is investigated in the present study of the wake-stabilised JFICF which are applicable for flares with values of  $R < 1.0$ .

## 2. Numerical models

### 2.1 Turbulent flow modelling

The modelling approach adopted in this study involves calculation of the flow field by solving Favre-averaged equations for the conservation of mass, momentum and energy, with the latter in its enthalpy form. The body force due to thermal buoyancy is incorporated by including the effect of gravitational acceleration in the momentum equation. The unknown terms in the averaged equations due to turbulence fluctuations were closed using three turbulence models, as described below.

Two levels of closure were used for modelling the Reynolds stresses  $\tau_{ij} = \rho \overline{u'_i u'_j}$ , these being first-order, or EVM, and second-order, or RSM, approaches. The basis of the linear EVM is the assumed isotropy of the turbulent viscosity  $\mu_t$ , based on which Reynolds stresses is considered to be proportional to the mean rate of strain. As such, the turbulent viscosity is expressed as  $\mu_t = C_\mu k^2/\varepsilon$ , where  $k$  is the turbulence kinetic energy,  $\varepsilon$  is its dissipation rate, and  $C_\mu$  is an empirical model constant. Linear EVM models, such as the standard  $k$ - $\varepsilon$  turbulence model [16], solve transport equations for  $k$  and  $\varepsilon$ , written in Favre-averaged form, as follows:

$$\frac{\partial}{\partial x_i}(\rho u_i k) = \frac{\partial}{\partial x_j} \left[ \left( \mu + \frac{\mu_t}{\sigma_k} \right) \frac{\partial k}{\partial x_j} \right] + \underbrace{(\mu + \mu_t) \left[ \frac{\partial u_i}{\partial x_j} \left( \frac{\partial u_i}{\partial x_j} + \frac{\partial u_j}{\partial x_i} \right) \right]}_{P_k} + \underbrace{\beta g_i \frac{(\mu + \mu_t)}{\text{Pr}_t} \frac{\partial T}{\partial x_i}}_{G_k} - \rho \varepsilon \quad (1)$$

$$\frac{\partial}{\partial x_i}(\rho u_i \varepsilon) = \frac{\partial}{\partial x_j} \left[ \left( \mu + \frac{\mu_t}{\sigma_\varepsilon} \right) \frac{\partial \varepsilon}{\partial x_j} \right] + C_{\varepsilon 1} \frac{\varepsilon}{k} (P_k + C_{\varepsilon 3} G_k) - C_{2\varepsilon} \rho \frac{\varepsilon^2}{k} \quad (2)$$

where  $P_k$  and  $G_k$  represent the generation of turbulence kinetic energy due to the mean velocity gradients and buoyancy, respectively. The value of the constant  $C_{\varepsilon 3}$  in Eq. (2) was determined based on the relation  $C_{\varepsilon 3} = \tanh|u_j/u_{cf}|$  [18]. The model constants applicable to Eqs. (1) and (2) are summarized in Table 1. These are typical theoretical/empirical constants that have been widely tested and used in various turbulent fluid flow simulations [16-18].

The assumption in the EVM that the Reynolds stresses are proportional to the mean rate of strain is valid only in flows with local spectral equilibrium. However, in most practical flows, for example in the JFICF, there is significant turbulence anisotropy due to recirculation and the presence of secondary flows. The linear EVM is not capable of adequately accounting for these phenomena, particularly the strong link between the turbulent stress and its production terms [17]. These shortcomings are attributable to the over-

prediction of the turbulent viscosity, and the use of an inappropriate turbulence length scale in the transport equations for  $k$  and  $\varepsilon$  [15]. This has led to the development of non-linear variants of the EVM (NEVM).

Among the NEVM, the RNG  $k$ - $\varepsilon$  model has demonstrated some success in computations of complex flow features. The modifications in the RNG  $k$ - $\varepsilon$  model include the replacement of the turbulent eddy viscosity by an effective viscosity,  $\mu_{eff}$ , defined as follows [17]:

$$d\left(\frac{\rho^2 k}{\sqrt{\varepsilon \mu_t}}\right) = 1.72 \frac{\hat{v}}{\sqrt{\hat{v}^3 - 1 + C_v}} d\hat{v} \quad (3)$$

where  $\hat{v} = \mu_{eff} / u_t$ ,  $C_v = 100$ , and  $u_t = u_{to} (\alpha_s, \Omega, k/\varepsilon)$ .  $u_{to}$  is the turbulent viscosity as used in the standard  $k$ - $\varepsilon$  model, whilst  $\Omega$  and  $\alpha_s$  are the swirl number and swirl constant, respectively. This modified viscosity leads to lower values of the model constants  $C_{\varepsilon 1}$  and  $C_{\varepsilon 2}$ , as given in Table 1, which have been found to be valid in both high and low Reynolds number flows. Furthermore, the RNG  $k$ - $\varepsilon$  model incorporates an extra strain-dependent correction term in the transport equation for  $\varepsilon$  represented by [17]:

$$R_\varepsilon = \frac{C_\mu \rho \eta^3 \left(1 - \frac{\eta}{\eta_o}\right) \varepsilon^2}{1 + \beta \eta^3} \frac{1}{k} \quad (4)$$

where  $\eta = Sk/\varepsilon$  is the relative strain parameter, and  $S = (S_{ij}S_{ji})^{1/2}$  is the strain rate. The term given in Eq. (4) is largely responsible for the difference in performance between the standard and the RNG models [17], which includes improved allowance for large strains and pervasive low Reynolds number effects. Both the standard and the RNG models have been very successful and widely used in various combustion and non-combustion process modelling applications where anisotropy of turbulence is less important [18-21].

Turbulence stress anisotropy can become significant in flows with complex strain fields. These are characterised by, amongst other things, strong pressure gradients, significant body forces (rotation and buoyancy) and three-dimensionality, all features that are present in the JFICF. Furthermore, the high temperatures in such flows, due to chemical reactions, lead to an increase in the kinematic viscosity and a consequent reduction in the turbulent Reynolds number. This in turn produces an increase in the turbulent stress anisotropy by delaying the return to isotropy [23]. In principle, NEVM models, such as the RNG  $k$ - $\varepsilon$  model, are capable of resolving some of the normal-stress anisotropy. However, they still retain a similar level of description and local determination of the Reynolds stresses as the EVM [19]. Therefore, even NEVM show some weaknesses in resolving the physical coupling between stresses and strains, as well as



the stress production resulting from the normal components of the turbulent stresses [17].

The simplest RANS closure model where anisotropy of the turbulent stress field is treated and modelled as a distinct physical process is the RSM. In addition to a transport equation for  $\varepsilon$ , the standard RSM solves [24] transport equations for the six components of  $\tau_{ij} = \rho \overline{u'_i u'_j}$

$$\begin{aligned} \frac{\partial}{\partial x_k} (\rho u_k \overline{u'_i u'_j}) = & \frac{\partial}{\partial x_k} \left( \mu \frac{\partial}{\partial x_k} (\overline{u'_i u'_j}) \right) - \rho \left( \overline{u'_i u'_k} \frac{\partial u_j}{\partial x_k} + \overline{u'_j u'_k} \frac{\partial u_i}{\partial x_k} \right) - 2\rho \Omega_k (\overline{u'_j u'_m} \varepsilon_{ikm} + \overline{u'_i u'_m} \varepsilon_{jkm}) \\ & + p \left( \frac{\partial u'_i}{\partial x_j} + \frac{\partial u'_j}{\partial x_i} \right) - 2\mu \frac{\partial u'_i}{\partial x_k} \frac{\partial u'_j}{\partial x_k} - \frac{\partial}{\partial x_k} \left[ \rho \overline{u'_i u'_j u'_k} + p (\overline{\delta_{kj} u'_i} + \overline{\delta_{ik} u'_j}) \right] - \rho \beta (g_i \overline{u'_j \theta} + g_j \overline{u'_i \theta}) \end{aligned} \quad (5)$$

The first three terms on the right hand side of Eq. (5) represent the contributions to Reynolds stress by molecular diffusion, turbulent stress production and system rotation, respectively. The last four terms represent the effects due to the pressure strain, turbulent dissipation, diffusion, and the production by buoyancy, respectively, which require modelling to close the set of the equations. In this study, the pressure-strain term in Eq. (5) was specified using the low Reynolds number modification to the linear pressure-strain correlation [25]. The turbulent diffusive transport term was modelled based on the scalar turbulent diffusivity approach [26], and the dissipation term was represented by  $\varepsilon_{ij} = (2/3)\rho\varepsilon\delta_{ij}$ . This approximation for the dissipation term may not be appropriate in the wall region of the release pipe due to the in-homogeneous character of the flow in this region. This deficiency is, however, compensated for by the pressure-strain term in Eq. (5) through which turbulence anisotropy in that region is accounted for [27]. Some of the important constants employed in this study are listed in Table 1. A more detailed description of the RSM and the standard set of constants are available [25-28].

## 2.2 Combustion modelling

The combustion process was modelled using the laminar flamelet concept [29] which relates the effect of turbulent fluctuations in flames to fluctuations in the mixture fraction and the scalar dissipation rate. Therefore, the flame was modelled based on the mixture fraction approach, and transport equations for the mixture fraction and its variance were solved, solutions to which served as inputs for calculating multiple flamelet profiles. The steady flamelet equations were solved for various values of the stoichiometric scalar dissipation  $\chi_{st}$  in the range 0.0001 to 33.5 s<sup>-1</sup>, and in steps of 2.5 s<sup>-1</sup>. A detailed description of the laminar flamelet approach employed and its application in modelling the combustion process in the JFICF has been provided elsewhere [30].

The justification for using the laminar flamelet model in this study is its ability to decouple the chemistry and flow field calculations, thus enabling an economic investigation of turbulent flames with detailed chemistry effects. The model has been shown to be valid in flows that favour the formation of flamelets, such as those with sufficiently large turbulence scales and low turbulence intensities [28]. Additionally, the laminar flamelet model is also valid in flows with room temperature reactants and low gas velocities, as well as in reactions near the mean stoichiometric contour. Interestingly, these flow conditions are similar to those found in the flames under investigation [31].

### 2.3 Radiation modelling

Radiant energy emission was accounted for using a finite-volume version of the discrete ordinates (DO) model [32]. This approach employs both the control volume and control angle integration techniques to solve the governing equation for the radiant intensity for a set of discrete directions in the total solid angle  $4\pi$ , which is more accurate than simpler models, such as the P1 model, and has been used routinely in the radiative heat transfer modelling of optically thin systems [19,33]. As a reasonable compromise between efficiency and accuracy in the DO model calculations, the  $S_2$  quadrature was used for the angular discretisation.

The weighted-sum-of-grey-gases model (WSGGM) was employed for calculating the absorptive and emissive contributions of the participating gaseous species based on the grey gas assumption [34]:

$$\varepsilon_0 = \sum_{i=0}^I a_{\varepsilon,i}(T)(1 - e^{-\kappa_i p L}) \quad (6)$$

where  $a_{\varepsilon,i}$  is the emissivity weighting factor which is a function of temperature,  $\kappa_i$  is the grey gas absorption coefficient,  $p$  is the sum of partial pressures of all absorbing gases, and  $L$  is the path length. A recent study of methane-air and oxy-fuel combustion at atmospheric pressure demonstrated that the radiation source term obtained with the WSGGM compares well with the more accurate non-grey method based on the narrow band, full-spectrum k-distribution approach [35]. The dominant radiant species from the combustion of natural gas, which generally gives a non-luminous flame, are  $H_2O$  and  $CO_2$  [26, 36]. Therefore, only the absorption coefficients of these species were taken into account in the present work.

### 3. Test conditions

Meaningful validation of reacting flow calculations against experimental data such as temperature,

turbulence properties and the distribution of combustion species are necessary. However, no single experimental study of methane or natural gas jet flames in cross-flow provides such a comprehensive data set. This has necessitated the requirement to compare results of important flow quantities from the present calculations against two experimental data sets. Therefore, in this study, two experimental configurations were modelled. The first is that of the flare experiments performed at the University of Alberta (UoA) using natural gas [37], whilst the second is the series of flare tests conducted at the Canada Energy Technology Centre (CETC) Flare Test Facility (FTF) in Ottawa [38], both using natural gas.

The flare experiments conducted at UoA were performed in a wind tunnel of dimensions  $2.44 \text{ m} \times 1.22 \text{ m} \times 11.8 \text{ m}$ . The flare pipe employed had inside and outside diameters of 22.1 and 24.7 mm (1"), respectively. The pipe was located 6.7 m from the entrance of the wind tunnel test section, and its exit protruded vertically 0.47 m into the tunnel. The flow conditions used consisted of burning a jet of natural gas (95%  $\text{CH}_4$ , 2.4%  $\text{C}_2\text{H}_6$ , 0.06%  $\text{C}_3\text{H}_8$ , 1.74%  $\text{N}_2$  and 0.81%  $\text{CO}_2$ ) at an exit velocity of  $1 \text{ ms}^{-1}$  in a cross-flow of  $3 \text{ ms}^{-1}$  ( $R = 0.07$ ). In this study, the results from UoA experiments are employed to validate the predicted temperatures which are utilised in representing the flame appearance. Table 2 provides a summary of the flow conditions investigated.

The working section of the FTF wind tunnel was of length 8.2 m and width 2.4 m, with the tunnel having an adjustable ceiling height starting at 1.5 m. A cylindrical pipe of length 0.61 m was employed to represent the flare release pipe. This pipe was located 2.4 m from the cross-flow inlet plane. Although the FTF experiments covered flare pipes of diameters 5.25 cm to 30.0 cm, in this study only flames from the 5.25 cm (2") diameter pipe are investigated, with the flames having been established by burning a jet of natural gas (95%  $\text{CH}_4$ , 2.1%  $\text{C}_2\text{H}_6$ , 0.2%  $\text{C}_3\text{H}_8$ , 1.8%  $\text{N}_2$  and 0.6%  $\text{CO}_2$ ). The velocities of the fuel jet ranged from 0.46 to  $5.3 \text{ ms}^{-1}$  under ambient wind speeds of up to  $12 \text{ ms}^{-1}$ . The Reynolds numbers based on the cross-flow velocity and the pipe diameter are shown in Table 2. FTF experimental data are available for the efficiency of the flames and the concentrations of major species. However, velocity and temperature field data were not obtained.

#### **4. Numerical solution and boundary conditions**

The computational domain employed was of dimensions  $2.4 \text{ m} \times 8.2 \text{ m} \times 1.5 \text{ m}$ . This translates to, for the case of the FTF, a domain that spans about 23d in the spanwise, 157d in the streamwise and 28d in the

vertical directions, where  $d$  is the inner diameter of the release pipe. The location of the release pipe was at a distance of  $46d$  from the cross-flow inlet plane. Figure 1 shows a schematic of a wake-stabilised JFICF with the origin of the co-ordinate system located at the exit plane of the release pipe.

In order to solve the governing equations, the computational domain and the release pipe were divided into several smaller sub-domains that were meshed using unstructured grids composed of hexahedral elements. Fine grid cells were placed near the pipe walls, the jet exit and near the upper and lower walls of the computational domain. The variation of the mesh was from an initial size of  $0.025d$ , with a growth factor of 1.05, reaching a maximum size of  $0.3d$  in the region spanning  $26d$  downstream and  $5d$  upstream in the spanwise direction. This ensured that the numerical grids nearest to the inlet pipe wall were at  $y^+ = 2.2$ . Further away from this region, relatively coarser grids were used by increasing the mesh size at a growth ratio of 1.1, reaching a maximum of  $2d$  over the remainder of the domain.

Boundary conditions were prescribed as follows. Although the interaction between the jet and the cross-flow is three-dimensional, the average flow field is symmetrical about the central,  $z=0$  plane [3]. Therefore, symmetry was assumed on this plane and only half of the complete domain was modelled. At the upstream  $y$ - $z$  plane, corresponding to the cross-flow inlet, a uniform velocity profile with a turbulence intensity of 1% was specified. Downstream of this plane, outflow conditions were implemented where zero values of the normal gradients of all flow variables were enforced. A uniform velocity profile was prescribed at the release pipe inlet, with a turbulence intensity of 5%. For the walls at the lower, upper and side boundaries of the computational domain, corresponding to the  $\pm x$ - $z$  planes and the  $x$ - $y$  plane, respectively, a slip wall boundary condition was specified. In the FTF experiments the wall temperature was maintained at or below 373 K. Therefore, in this case, a fixed temperature of 373 K was also specified on the walls.

All the descriptive flow equations were discretised without time dependent terms using the second-order upwind scheme implemented in the ANSYS-FLUENT 13.0 CFD code [28] and which gives details of all the sub-models used. The use of a steady state calculation method was warranted by the fact that after the initial mixing, the overall combustion process and the production of chemical species occurs in a steady-like manner [37]. The SIMPLE algorithm [39] was used for pressure-velocity coupling, and the chemical kinetic mechanism employed was GRI-MECH 3.0 [40].

The accuracy of the numerical solution obtained was assessed using two main approaches. The first

involved evaluating the convergence of the fluid flow equations solved and the second was based on a grid dependency study. Solution convergence was obtained when the sum of the normalised residuals for equations of continuity and momentum fall below value of  $10^{-5}$ , for enthalpy and species below  $10^{-7}$  and for of radiation below  $10^{-9}$ . To ensure the results from the numerical calculations were not sensitive to the grid employed, initial solution was conducted with a fine mesh consisting of 750,00 grids. This grid was refined in the region spanning 26d downstream and 5d upstream of the jet exit, producing a finer mesh comprising a total of 1,200,000 grids. Comparison of results from the calculations obtained with the two sets of grids show less than 5 percent difference in the predicted temperature and species profiles. Subsequently, the finer grid was employed for the main calculations whose results are reported and discussed in the following sections.

## **5. Results and discussion**

In this section, predictions obtained from the three turbulence models for the principal flow features of interest are presented and discussed for the cases of both UoA and FTF tests. This starts with a description of the flame appearance, following which the predicted velocity and vorticity fields are analysed in the light of the trends reported for the UoA experimental data. Subsequently, an analysis of the ability of the RSM and RNG turbulence models to predict the planar flame zone in the wake of the release pipe is performed. Finally, a comparison of the predicted flare efficiencies with the FTF experimental data is presented.

### **5.1 Flame appearance**

Photographs of flame appearance are in terms of its luminosity, which is caused by excited species and soot [31]. Flame images are widely used to measure flame length which can give an indication of the size of the high-temperature zone, in particular for blue flames such as those of methane, and the residence time available for pollutant formation within the flame [41]. Comparing the computed flame region and its luminosity field from experiment has long been known to be difficult. [42]. However, the non-linear dependence of the radiation heat flux on the flame temperature suggests that temperature would be a good marker for radiation, and hence the visible flame region. This assumption has been found to be reasonably accurate in methane flames with low soot concentrations [14].

Therefore, the flame appearance discussed here is in terms of the half-mean temperature rise relative

to the ambient, which was employed in discussing the UoA experimental temperature contours [37]. This is defined as:

$$\frac{T - T_{amb}}{T_{max} - T_{amb}} = 0.5 \quad (7)$$

where  $T$  is the mean temperature,  $T_{amb}$  is the mean ambient air temperature, and  $T_{max}$  is the maximum mean temperature of the flame.

Side and top views of the predicted average half-mean temperature contours for the UoA flame, i.e. flame 1, are presented in Fig. 2(a-c). These represent the predictions obtained with the standard  $k-\varepsilon$ , the RNG  $k-\varepsilon$  and the Reynolds stress turbulence models, abbreviated in the figure by SKE, RNG and RSM. Fig. 2 demonstrates that all three models reproduce the general appearance of the flame [6,37]. This includes the flame trajectory and its orientation relative to the pipe exit, as well as the presence of two flame zones in the top view, starting from  $y/d = -1.0$ . These two zones show two peak temperatures which are, necessarily, symmetric in the transverse direction.

Furthermore, Fig. 2 shows that, similar to the short-exposure photographs [37], the simulations resolve the inclination of the flame as proximately 10 degrees to the horizontal. However, the offset of the flame from the pipe exit by approximately 5 diameters in the photographic images is not resolved by the three turbulence models, with the models predicting the flame to be stabilised directly on the pipe lip. Similarly, the size of the flame attached to the release pipe, below the plane of the jet exit, is significantly under-predicted by all the models, and in particular by the standard  $k-\varepsilon$  model. This region corresponds to the planar recirculation zone and, as discussed in Section 5.5, under certain flow conditions the RSM is capable of resolving this flame attachment reasonably well.

An established feature of the wake-stabilised JFICF is its characteristic three-zone structure [6,10]. These zones are the planar flame zone attached to the release pipe, the symmetric tail flame, and a dark neck flame, or transition zone connecting the latter two zones, as illustrated in Fig.1. It is apparent from Fig. 2(a-b) that the RNG and the standard  $k-\varepsilon$  turbulence models capture the first two zones adequately. However, only the predictions from the RSM resolve all three zones, including a small neck flame region, as seen in Fig. 2(c). The location of this zone corresponds to the region where the shearing of the jet fluid is significant, with the strong shear and acceleration of the jet fluid in this region inducing large Reynolds stresses and stress gradients [9]. Evidently, the RSM is able to resolves this phenomenon reasonably well,

as indicated by its prediction of the neck flame zone. The poor prediction of this zone by the RNG and standard  $k-\varepsilon$  turbulence models can be attributed to the inability of these models to account accurately for the normal components of the Reynolds stresses.

## 5.2 Velocity profiles

To examine the important interactions between the jet and the cross-flow in the wake region, variations in the transverse profiles of the mean streamwise (U) and vertical (V) velocity components in the region close to the jet exit ( $x/d = 1.64$ ) are presented in Fig. 3 for flame 1. This shows that the velocity profiles are mostly uniform away from the symmetry plane in the flow, indicating the presence of an undisturbed cross-flow. At  $y/d = 2$ , i.e. just above the jet exit, the three turbulence models predict velocity profiles that capture the expected up-streaming effect of the jet fluid on the cross-flow as shown in Fig. 3(a). This effect produces a sudden increase in the cross-flow velocity by approximately 31%, which is consistent with the 40% increase reported experimentally for a propane JFICF with  $R = 0.04$  [10]. The V velocity profiles resolve the expected monotonic decrease from the peak positive values on the plane of symmetry, to almost negative values elsewhere as shown in Fig. 3(b). Although the three turbulence models predict similar U and V velocity trends above the jet exit, the velocity profiles obtained from the RNG  $k-\varepsilon$  model and the RSM are in closer agreement.

In the region of the jet exit ( $y/d = 0$ ), the U velocity profiles dip and reach a minimum a short distance away from the symmetry plane ( $z/d = 0.5$ ). These profiles then increase with  $z/d$ , reaching a peak at  $y/d = 1.0$ . The V velocity profiles predicted by the three turbulence models are also comparable with peak values occurring on the plane of symmetry shown in Fig. 3(d). Again, the velocity profiles predicted by the RSM and the RNG  $k-\varepsilon$  model are in close agreement. These two models also predict a more sudden drop in both the U and V velocity profiles than the standard  $k-\varepsilon$  model. The failure of the latter model to resolve this trend can be attributed to its spurious generation of turbulence energy and viscosity, which degrade the solution of the predicted velocity. The sudden drop in velocities in this region suggests the occurrence of vortex breakdown, which has also been observed in an LES study of non-reacting round jets in a cross-flow [43].

Below the jet exit ( $y/d = -1.4$ ), the three turbulence models predict similar U velocity profiles, as shown in Figure 3(e). In this region of normal wake flow, the U velocity profile dips close to the symmetry

plane, while the V velocity profile, Fig. 3(f), shows a peak value. These trends are consistent with previous experimental observations [10]. It should also be noted that the transition of the V velocity profiles from positive values on the plane of symmetry to negative values in the wake region is an indication of the dominance of recirculation vortices caused by vortex breakdown. As is evident in Fig. 3(f), the RSM resolves this phenomenon more accurately than the standard and RNG  $k-\varepsilon$  turbulence models.

### 5.3 Turbulence intensity profiles

The evolution of the streamwise turbulence characteristics as the flame advects downstream is examined through the profiles of predicted turbulence intensity. This variable has been shown to have an analogous behaviour to the Reynolds shear stress and turbulence production [10]. Vertical profiles of the normalized turbulence intensities at two downstream locations on the plane of symmetry ( $x/d = 1.62$  and  $22$ ) for flame 1 are presented in Figure 4, based on which the following features are worthy of note: (i) At the location near the jet exit the turbulence intensity profile is characteristic of jets with the peak value at the centre-line decreasing away from this location (Fig. 4(a)); (ii) The free stream turbulence intensities below the jet exit plane are higher, by approximately 85%, than those above that plane, further illustrating that vortex stretching is significant in the wake region. This finding is consistent with the experimental data of Andeopoulos and Rodi [3] although their measurements were made with cold air flows; (iii) As the flow moves further downstream, the differences in the turbulence intensities between the upper and lower half of the jet decay. These approach a value of approximately 5% at  $x/d = 22$ , with the standard  $k-\varepsilon$  model predicting a relatively higher peak intensity, as shown in Fig. 4(b); (iv) Further downstream, the peak turbulence intensity decreases, and the vertical location above the jet exit where this peak occurs shifts to the upper half of the flame trajectory. For example, for the profiles at  $x/d = 1.62$  and  $22$ , the peak intensities correspond to locations where  $y/d = 0.4$  and  $3.6$ , respectively. This shift is due to the rise of the jet with downstream distance, resulting in an increase in the vertical height of the peak intensity with distance.

The general trends in the turbulence intensity distribution described above were captured by all three turbulence models. Nevertheless, it is only the RSM that predicts the expected turbulence fluctuations near the jet exit, consistent with the experimental observations of Huang and Wang [10] using propane flames.



In comparison, the RNG and standard  $k-\epsilon$  models predict an initially unperturbed turbulence profile that increases abruptly near the jet centre-line. Due to the over-prediction of turbulence production by the standard  $k-\epsilon$  model, this model also predicts a higher peak intensity in comparison with the RSM and the RNG  $k-\epsilon$  approaches whose predicted peak turbulence intensities are in closer agreement.

Furthermore, and in agreement again with the experimental findings of Huang and Wang [10] with a propane flame, the predicted peak turbulence intensity in the wake of the jet ( $y/d = 0$ ) is higher than that in the wake of the pipe ( $y/d = -1.4$ ). This is shown in Fig. 5(a-b) which gives predictions of the transverse distribution of the normalized turbulence intensity in the wake region. Again, it is the RSM and RNG  $k-\epsilon$  models that resolve this subtle difference more accurately, with the standard  $k-\epsilon$  model predicting similar and much higher turbulence intensities in both the jet and pipe wake.

#### 5.4 Vorticity fields

Regions of high vorticity usually coincide with the location of coherent structures in the flow field. A clear visualisation of these features in the wake of the release pipe is given in terms of the normalized streamwise vorticity contours presented in Fig. 6 for flame 1. The negative vorticity contours delineate the downwash affected region that leads to a depression of the velocity profiles in the jet and pipe wake, as discussed in Section 5.2. The compact region of concentrated vorticity is observed to spread rapidly, confirming the occurrence of vortex break down in the wake zone. Experiments suggest the secondary flame zone that forms below the pipe exit originates from the vorticity concentrated in this region [10].

Below the negative vorticity zone in the wake of the pipe, there is a region of positive vorticity. The change in sign of the vorticity in this region signifies the change in the flow pattern due to flow reversal and recirculation, which only the RSM accurately resolves, as shown in Figure 6(c). Overall, and compared to the solutions obtained with the RNG and RSM, Figures 6(b) and (c) respectively, the standard  $k-\epsilon$  model predicts a more rapid decay of the vorticity strength as the flow progresses downstream, resulting in a smaller vorticity affected region.

An explanation for this is likely the inability of the standard  $k-\epsilon$  model to account for the production of system rotation, which decreases the dissipation of turbulence energy even in isotropic turbulence [27]. On the other hand, in the RSM, the transport equation for the Reynolds stress accounts for this mechanism in the rotational production term, through which the Reynolds stresses are redistributed amongst other

components. In the RNG  $k-\varepsilon$  model, the additional strain parameter in the transport equation for the dissipation rate of  $k$  performs the role of decreasing the rate of dissipation. As a result, both the RSM and RNG  $k-\varepsilon$  models predict similar positive vorticity regions. All the above findings are indications that the RSM and RNG  $k-\varepsilon$  turbulence models provide better predictions of the main flow features of the wake-stabilised JFICF. Therefore, it is instructive to determine in exactly what way these two models differ in resolving the more complex features resulting from changes in flow conditions, such as the secondary flame zone in the wake of the release pipe. This aspect is discussed in the following section.

### 5.5 Influence of flow conditions

In this section, the ability of the RSM and RNG  $k-\varepsilon$  turbulence models to reproduce the effect of changes in the flow conditions on the size of the planar flame zone attached to the release pipe is investigated. The cross-flow velocity ( $u_{cf}$ ) is one of the main flow variables that significantly influences the flow structures and the burning efficiency characteristics of a flame, for example as shown by Johnson and Kostiuk [12]. In this respect, the effect of changing  $u_{cf}$  and the fuel jet velocity ( $u_j$ ) is examined. Additional calculations were carried out, based on the FTF configuration, with similar  $u_{cf}$  and different  $u_j$ —flames 6 and 7 of Table 2.

From this table, it is observed that there is an approximately four-fold reduction in  $u_j$  from flames 6 to 7, producing a significant decrease in the value of  $R$  from 0.092 to 0.005. The flow conditions in these runs are such that the flame is cross-flow dominated. Experimental studies of natural gas JFICF have shown that a significant increase in the cross-flow velocity [12], or a large reduction in the jet exit velocity [6], i.e. a very low value of  $R$ , produces an increase in the size of the recirculation vortex on the leeward side of the release pipe. It has also been suggested that these vortices are responsible for the flow of jet fluid into the wake region, resulting in an increase in the size of the planar flame zone attached to the release pipe. Under these flow conditions, the symmetric tail flame zone becomes narrower and shorter, while the neck of the flame zone disappears. The significance of these geometric transformations in reducing the efficiency characteristics of the flame is well documented [12,44].

Comparisons of the RNG  $k-\varepsilon$  and RSM predictions of the average temperature contours for flames 6 and 7 are presented in Figs. 7 and 8, respectively. It is observed that all of the geometric changes mentioned above are reproduced by the RSM, e.g. comparing Figs. 7(b) and 8(b). In fact, the size of the

planar flame zone attached to the pipe in flame 7 extends up to 3.5d below the pipe exit, and the peak temperature in this region is similar to that in the tail flame. These observations are consistent with those made in relation to the experimental data [37]. The temperature contours in Fig. 8(b) show that due to the significant decrease in  $u_j$ , the fuel jet is bent over enough by the cross-flow to cause most of the tail flame to reside below the pipe exit plane. On the other hand, a comparison of Figs. 7(a) and 8(a) reveals that the RNG  $k-\varepsilon$  turbulence model does not resolve these expected transformations in the flame features, nor the planar flame zone attached to the release pipe. Notwithstanding the dominance of the cross-flow due to the significant decrease in  $u_j$ , the RNG  $k-\varepsilon$  model also predicts essentially the same size of planar flame zone for the flow conditions of flames 6 and 7.

The main flow feature on the leeside of the release pipe is caused by the reduced pressure within the recirculation vortices in the downwash wake region. This is created largely due to the negative (downwash) velocity and the change in orientation of the cross-flow as it by-passes the pipe walls. The resulting flow separation and counter-rotating vortices create a low pressure wake and a highly turbulent free shear layer with significant turbulence anisotropy. Consequently, the transport of momentum is largely governed by the wall normal stress components. This phenomenon is accounted for explicitly in the RSM transport equations through the pressure-strain correlation and the stress production terms, see Eq. (5). Consequently, at very low values of  $u_j$  where these phenomena acquire more significance, the RSM is able to resolve the complex flow features reasonably well. Hence, it better predicts the planar flame zone attached to the release pipe. The superiority of the RSM over the  $k-\varepsilon$  model in predicting swirling flows has also been discussed in [21] for nonreacting flows in baffled stirred vessels.

## 5.6 Combustion efficiency

Flare performance is usually determined in terms of the combustion efficiency or carbon conversion efficiency ( $\eta_t$ ), which is defined [44] as:

$$\eta_t = \frac{\text{net mass rate of } CO_2}{\text{net mass rate of } (CO_2 + CO + CH_4)} \quad (8)$$

In the experiments, the conversion efficiency can be calculated by replacing the net rate terms in Eq. (8) by the measured product concentrations. These species concentrations are measured with on-line gas analyzers. Flame ionization detectors are used for CH<sub>4</sub> measurements and nondispersive infrared analyzers are used for CO<sub>2</sub> and CO. All of the analyzers employed have an uncertainty of 1% of their full-scale

reading. Therefore an estimated error in the conversion efficiency is less than approximately 0.6% [37-38, 44].

In flares where the conversion efficiency is close to 100%, the combustion performance is preferably discussed in terms of the inefficiency, which is defined as  $1 - \eta_i$ . Previous experimental studies have established that the efficiency of flare combustion has a strong dependence on the cross-flow velocity [7,44]. Therefore in the following, the capability of the three turbulence models to capture this dependency is examined.

A comparison of the predictions of the flare combustion efficiency and inefficiency obtained using the three turbulence models with the FTF experimental data is presented in Fig. 9. As shown in Figure 9 (a), the results indicate a negative linear correlation of the combustion efficiency with  $u_{cf}$ , which is consistent with the experimental observations [44]. This trend implies a decrease in flare efficiency with an increase in values of  $u_{cf}$ . Even though there are no experimental data at the limiting cross-flow velocity ( $12 \text{ ms}^{-1}$ ), it is evident from the figure that the RSM and RNG  $k-\varepsilon$  turbulence models predicted efficiencies that are more consistent with the best-fit curve through the measured efficiencies.

In contrast, Fig. 9(b) shows that the combustion inefficiency has a positive linear correlation with  $u_{cf}$ . The increase in inefficiency at higher values of  $u_{cf}$  is believed to be a consequence of an increase in the quantity of fuel that escapes from the pipe exit without burning [37]. The results show that the three turbulence models predict flare combustion efficiencies and inefficiencies that are generally in good agreement with the experimental data, as well as with its best-fit curve. It is observed that no single turbulence model can be identified as predicting flare efficiencies that are consistently closer to the experimental data. However, at the limiting condition of the highest value of  $u_{cf}$ , it is the RSM predictions of efficiency and inefficiency that are more consistent with the best-fit curve and are therefore judged to be most accurate, while the standard  $k-\varepsilon$  model is the least accurate.

## 6. Conclusions

The ability of three turbulence models to predict the important flow features in the wake-stabilised JFICF as a model of flares has been investigated. The models employed were a low-Reynolds-number extension of a differential second-moment turbulence closure, and linear and non-linear eddy viscosity models, based on the standard and the RNG  $k-\varepsilon$  turbulence model.

The standard  $k-\varepsilon$  and the RNG  $k-\varepsilon$  models predicted two of the three established flame zone structures in the wake-stabilised JFICF. Only the RSM resolved all three structures, namely the planar flame zone attached to the release pipe, the symmetric tail flame, and the neck flame.

All the models predict similar velocity profiles in most of the flow domain, except in the wake region where the predictions of the RSM and RNG  $k-\varepsilon$  models are in closer agreement. These two models also predicted similar turbulence intensities below the jet exit plane, while the standard  $k-\varepsilon$  model showed a significant over-prediction by comparison. Furthermore, it has been shown that in the cross-flow dominated flow regime, the RSM resolves the planar flame zone attached to the release pipe in the wake region. This flow feature is not captured by the standard and the RNG  $k-\varepsilon$  turbulence models.

Although none of the three turbulence models predicted combustion efficiencies that are consistently in closer agreement with experimental data, at the limiting condition of the highest value of  $u_{cf}$ , the RSM predictions of efficiency and inefficiency are more consistent with the best-fit curve through the experimental data, and are therefore judged to be more accurate.

Overall, while all three turbulence models predict the gross features of these flames, only the RSM resolved the more complex flow features in agreement with experimental data. The RSM resolved both the qualitative and quantitative characteristics of wake-stabilised flames observed in experiments that were not evident in predictions made with the other two turbulence models. Therefore, the RSM can be used with confidence to model wake-stabilised flames in the range of operating conditions discussed in this paper.

### **Acknowledgement**

M.S. Lawal acknowledges the financial support of the Nigerian Government provided through the Petroleum Technology Development Fund's Overseas Scholarship Scheme (PTDF-OSS).

## References

- [1] Branco DAC, Szklo AS, Schaeffer R. CO<sub>2</sub>e emissions abatement costs of reducing natural gas flaring in Brazil by investing in offshore GTL plants producing premium diesel, *Energy* 2010; 35:158-167
- [2] Khalilpour R, Karimi IA. Evaluation of utilization alternatives for stranded natural gas, *Energy* 2012; 40:317-328.
- [3] Huang RF, Chang JM. Coherent Structures in a Combusting Jet in Cross-flow. *AIAA* 1994; 32: 1120-5.
- [4] Andeopoulos J, Rodi W. Experimental Investigation of Jets in a Cross-flow. *J Fluid Mech* 1984; 138:93-127.
- [5] Birch AD, Brown DR, Fairweather M, Hargrave GK. An Experimental Study of a Turbulent Natural Gas jet in a Cross-Flow. *Combust Sci Technol* 1989; 66: 217 - 32.
- [6] Gollahalli SR, Nanjundappa B. Burner Wake Stabilized Gas Jet Flames in Cross-Flow. *Combust Sci Technol* 1995; 109: 327 - 46.
- [7] Gogolek P, Caverly A, Schwartz R, Seebold J, Pohl J. Emission from Elevated Flares - A Survey of the Literature. *AFRC 2010 Pacific Rim Combustion Symposium*, IFRF: Maui, USA, 2010.
- [8] Barlow RS, Frank JH. Effects of turbulence on species mass fractions in methane/air jet flames. *Proceedings Combustion Institute* 1998; 27: 1087-95.
- [9] Huang RF, Yang MJ. Thermal and concentration fields of burner-attached jet flames in cross flow. *Combust Flame* 1996; 105:211-24.
- [10] Huang RF, Wang SM. Characteristic flow modes of wake-stabilized jet flames in a transverse air stream. *Combust Flame* 1999; 117:59-77.
- [11] Gogolek PEG, Hayden ACS. Performance of flare flames in a crosswind with nitrogen dilution. *Journal of Canadian Petroleum Technology* 2004; 43: 43- 7.
- [12] Johnson MR, Kostiuk, LW. A parametric model for the efficiency of a flare in crosswind. *Proceedings Combustion Institute* 2002; 29: 1943-50.
- [13] Smith P, Sour Gas Flare simulations. Institute for clean and secure energy, The University of Utah, Utah, USA 2009. [www.flaresimulations.org/arc/](http://www.flaresimulations.org/arc/) (last accessed 19 October 2012).
- [14] Fairweather M, Jones WP, Lindstedt, RP, Marquis AJ. Predictions of a turbulent reacting jet in a cross-flow. *Combust Flame* 1991; 84: 361-75.

- [15] Yang W, Blasiak W. Numerical study of fuel temperature influence on single gas jet combustion in highly preheated and oxygen deficient air, *Energy* 2005; 30:385–398.
- [16] Launder BE, Spalding DB. Application of the energy-dissipation models of turbulence to the calculation of flow near a spinning disc. *Comput Methods Appl Mech Engg* 3 1974; 2: 269-89.
- [17] Yakhot V, Orszag SA. Development of Turbulence Models for Shear Flows by a Double Expansion Technique. *J Sci Comput* 1986: 1: 3-5
- [18] Henkes RAWM, Van der flugt M, FF, Hoogendoorn, CJ. Natural Convection Flow in a Square Cavity Calculated with Low-Reynolds-Number Turbulence Models. *Int J Heat Mass Transfer* 1991; 34:1543-57.
- [19] Mi J, Li P, Zheng C. Impact of injection conditions on flame characteristics from a parallel multi-jet burner. *Energy* 2011; 36: 6583-6595.
- [20] Yeh CP , Du SW, Tsai CH, Yang RJ. Numerical analysis of flow and combustion behavior in tuyere and raceway of blast furnace fueled with pulverized coal and recycled top gas, *Energy* 2012; 42: 233-240.
- [21] Ammar M, Chtourou W, Driss Z, Abid MS. Numerical investigation of turbulent flow generated in baffled stirred vessels equipped with three different turbines in one and two-stage system. *Energy* 2011; 36:5081-5093.
- [22] Pope SB. *Turbulent Flows*. Cambridge: Cambridge University Press, UK; 2000.
- [23] Janicka J. A reynolds-stress model for the prediction of diffusion flames. *Proceedings Combustion Institute* 1988; 21: 1409-17.
- [24] Gibson MM, Launder BE. Ground effects on pressure fluctuation in the atmospheric boundary layer. *J Fluid Mech* 1978; 86: 491-511.
- [25] Launder BE, Shima N. Second-moment closure for the near-wall sub-layer - Development and application. *AIAA* 1989; 27: 1319-25.
- [26] Lien FS, Leschziner MA. Assessment of turbulence-transport models including non-linear RNG eddy-viscosity formulation and second-moment closure for flow over a backward-facing step. *Comput Fluids* 1994; 23: 983-1004.
- [27] Hanjalic K. Second-Moment Turbulence Closures for CFD: Needs and Prospects. *Int J Comput Fluid Dyn* 1999; 12: 67 - 97.

- [28] Fluent Inc. FLUENT 6.3 User's Guide, [www1.ansys.com/customer/content/documentation/121/fluent/flth.pdf](http://www1.ansys.com/customer/content/documentation/121/fluent/flth.pdf) (last accessed 19 October 2012).
- [29] Peters N. Laminar flamelet concepts in turbulent combustion. *Proceedings Combustion Institute* 1998; 21: 1231-50.
- [30] Lawal MS, Fairweather M, Ingham DB, Ma L, Pourkashanian M, Williams A. Numerical study of emission characteristics of a jet flame in a cross-flow. *Combust Sci Technol* 2010; 182: 1491 - 510.
- [31] Coats CM. Coherent structures in combustion. *Prog in Energ Combust* 1996; 22: 427-509.
- [32] Chui EH, Raithby GD. Computation of radiant heat transfer on a non-orthogonal mesh using the finite-volume method. *Num Heat Transfer B* 1993; 23: 269 -88.
- [33] Kangwanpongpan T, Silva RC, Krautz HJ. Prediction of oxy-coal combustion through an optimized weighted sum of gray gases model, *Energy* 2012; 41:244-251.
- [34] Modest MF. *Radiative Heat Transfer*. London: Academic Press. UK; 2003.
- [35] Porter R, Liu, F, Pourkashanian M, Williams A, Smith D. Evaluation of solution methods for radiative heat transfer in gaseous oxy-fuel combustion environments. *J Quant Spectrosc RA* 2010; 111: 2084-94.
- [36] Cook DK, Fairweather M, Hammonds J, Hughes DJ. Size and radiative characteristics of natural gas flares. Part 2- Empirical model. *Trans. IChemE, Chem. Eng. Res. Des.* 1987;65:318–325.
- [37] Kostiuk LW, Johnson MR Thomas G; University of Alberta. University of Alberta Flare Research Project Final Report 2004, Alberta, Canada.
- [38] Gogolek P, Hayden ACS, Madrali S. Performance and Speciation of Solution Gas Fares Tested in the CANMET Flare Test Facility-Final Report. CETC report to PTAC 2001. Natural Resource Canada, CANMET Energy Technology Centre, Ottawa, Canada.
- [39] Pantakar SV. *Numerical Heat Transfer and Fluid Flow*. New York: McGraw Hill, USA; 1980.
- [40] Smith GP, Golden DM, Frenklach M, Moriarty NW, Eiteneer B, Goldenberg M et al. GRI 3.0 MECH; [www.me.berkeley.edu/gri\\_mech/](http://www.me.berkeley.edu/gri_mech/) (last accessed 19 October 2012).
- [41] Dong LL, Cheung CS, Leung CW. Combustion optimization of a port-array inverse diffusion flame jet. *Energy* 2011; 36:2834-2846.
- [42] Hottel HC, Broughton FP. Determination of true temperature and total radiation from luminous gas



flames. *Ind Eng Chem* 1932; 4:166-75.

[43] Yuan LL, Street RL, Ferziger JH. Large-eddy simulations of a round jet in cross-flow. *J Fluid Mech* 1999; 379: 71-104.

[44] Johnson MR, Kostiuk, LW. Efficiencies of low-momentum jet diffusion flames in crosswinds. *Combust Flame* 2000; 123: 189-200.

## **Table Legends**

Table 1: Summary of the turbulence model constants.

Table 2: Summary of the flow conditions investigated.

## Figure Legends

**Figure 1** Schematic of the structure of a wake-stabilised jet flame in a cross-flow and the co-ordinate system employed.

**Figure 2** Predicted half-mean temperature contours for flame 1 on the x-z plane and the plane of symmetry for calculations with (a) SKE, (b) RNG and (c) RSM models (scale applies to all figures).

**Figure 3** Predicted transverse profiles of mean velocity in the near wake region ( $x/d = 1.64$ ) at different vertical locations for flame 1: (a - b) in the bend of the jet at  $y/d = 2$ , just above the pipe exit, (c - d) in the wake of the jet at  $y/d = 0$ , near the pipe exit, and (e - f) in the wake of the release pipe at  $y/d = -1.4$ , just below the pipe exit.

**Figure 4** Vertical profiles of predicted averaged normalized turbulence intensity for flame 1 at two downstream locations on the plane of symmetry: (a)  $x/d = 1.62$ , and (b)  $x/d = 22$ .

**Figure 5** Transverse profiles of predicted averaged normalized turbulence intensity in the wake region of flame 1: (a) wake of the jet at  $y/d = 0$ , and (b) wake of the pipe at  $y/d = -1.4$

**Figure 6** Contours of the predicted normalized x-vorticity on the plane of symmetry: (a) SKE, (b) RNG, and (c) RSM models for flame 1.

**Figure 7** Predicted temperature contours on the plane of symmetry for calculations with (a) RNG and (b) RSM. The flow conditions are for flame 6:  $u_j = 1.94 \text{ ms}^{-1}$ ,  $u_{cf} = 5.19 \text{ ms}^{-1}$ .

**Figure 8** Predicted temperature contours on the plane of symmetry for calculations with (a) RNG and (b) RSM. The flow conditions are for flame 7:  $u_j = 0.46 \text{ ms}^{-1}$ ,  $u_{cf} = 5.2 \text{ ms}^{-1}$ .

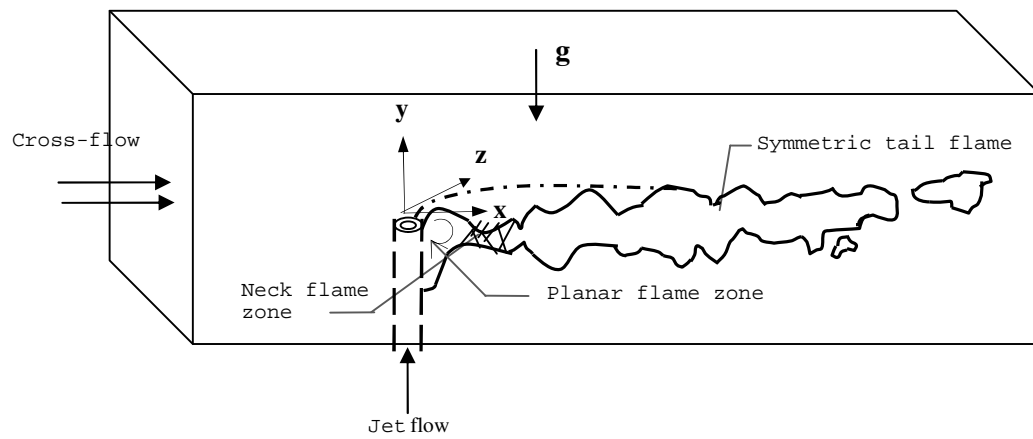
**Figure 9** Comparison of experimental flame combustion efficiency and inefficiency at different cross-flow velocities with predictions obtained from the three turbulence models: (a) combustion efficiency, and (b) combustion inefficiency. Straight line represent best-fit curve through the experimental data.

Table 1: Summary of the turbulence model constants.

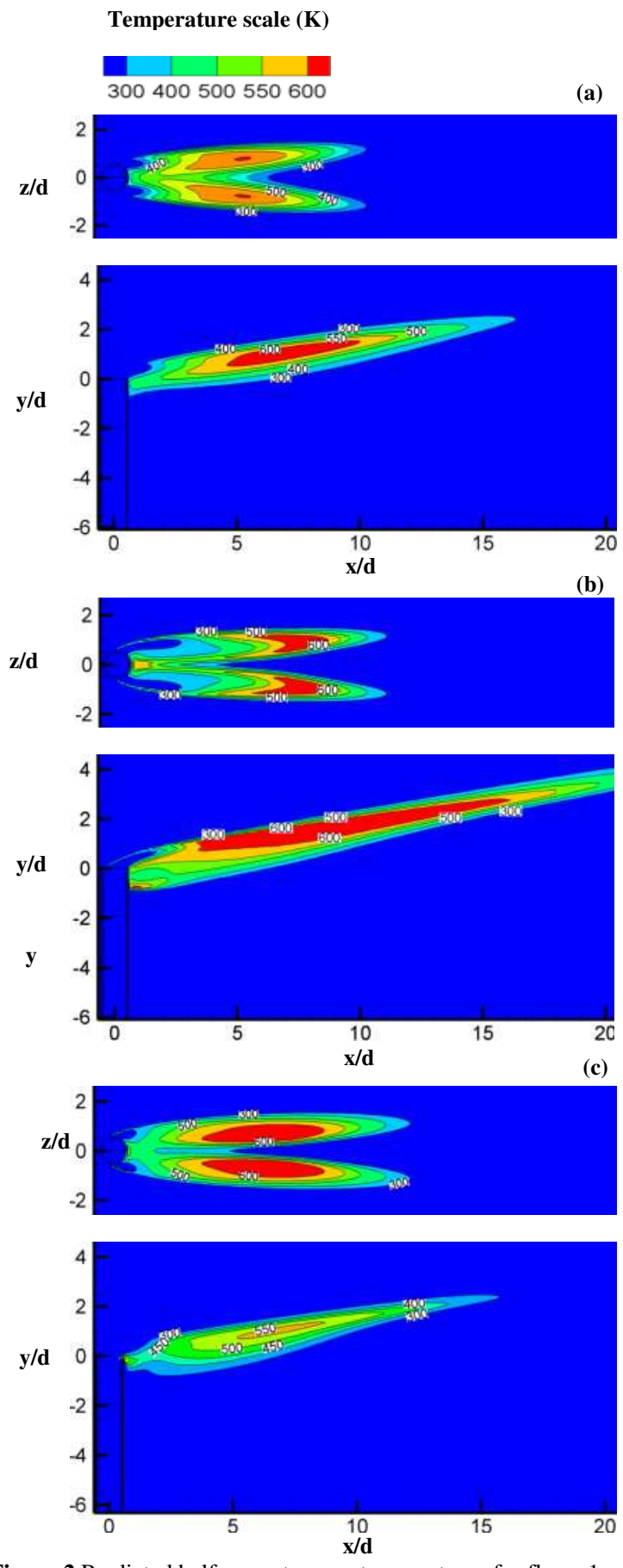
Model	$C_\mu$	$C_{\varepsilon 1}$	$C_{\varepsilon 2}$	$\sigma_k$	$\sigma_\varepsilon$	$\beta$	$\eta_o$
Standard $k$ - $\varepsilon$	0.09	1.44	1.94	1.0	1.17	0.012	-
RNG $k$ - $\varepsilon$	0.085	1.42	1.68	0.718	0.718	0.012	4.38
RSM	0.09	1.44	1.94	0.82	1.0	0.012	-

Table 2: Summary of the flow conditions investigated.

Flame	$u_j$ (ms <sup>-1</sup> )	$u_{cf}$ (ms <sup>-1</sup> )	$d_j$ (cm)	$Re_w$	$R$	Remarks
1	1.00	3.00	2.21	3364	0.070	UoA
2	5.28	8.45	5.25	28292	0.256	FTF
3	5.37	6.85	5.25	22935	0.040	FTF
4	5.28	12.50	5.25	41852	0.120	FTF
5	2.03	1.97	5.25	6596	0.700	FTF
6	1.94	5.19	5.25	17377	0.092	FTF
7	0.46	5.20	5.25	17410	0.005	FTF
8	3.75	5.22	5.25	17478	0.340	FTF
9	2.52	2.10	5.25	7031	0.950	FTF



**Figure 1** Schematic of the structure of a wake-stabilised jet flame in a cross-flow and the co-ordinate system employed.



**Figure 2** Predicted half-mean temperature contours for flame 1 on the x-z plane and the plane of symmetry for calculations with (a) SKE, (b) RNG and (c) RSM models (scale applies to all figures).

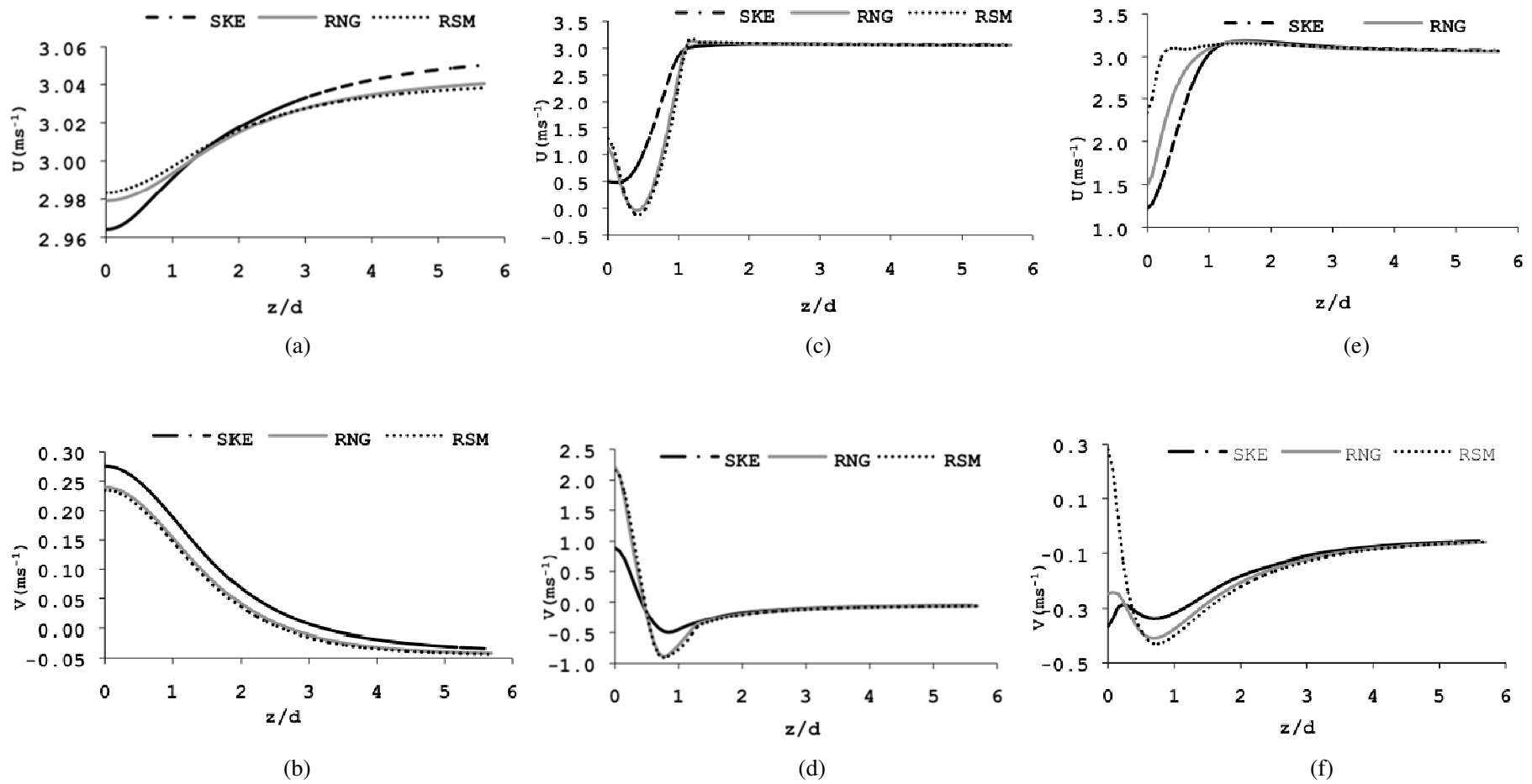
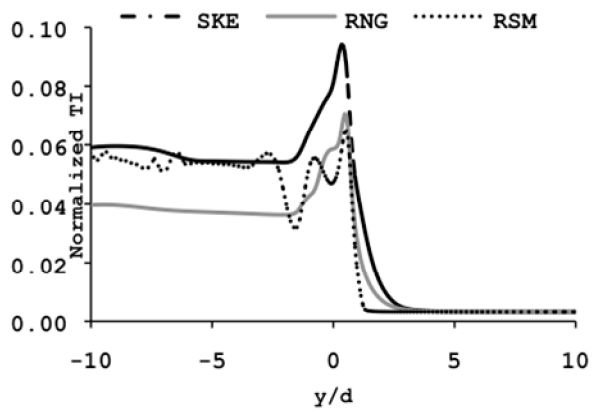
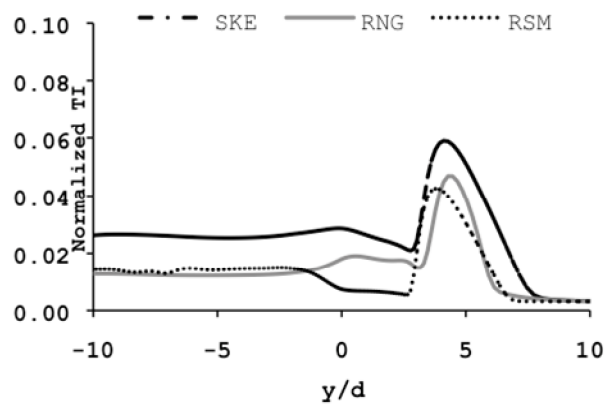


**Figure 3** Predicted transverse profiles of mean velocity in the near wake region ( $x/d = 1.64$ ) at different vertical locations for flame 1: (a - b) in the bend of the jet at  $y/d = 2$ , just above the pipe exit, (c - d) in the wake of the jet at  $y/d = 0$ , near the pipe exit, and (e - f) in the wake of the release pipe at  $y/d = -1.4$ , just below the pipe exit.



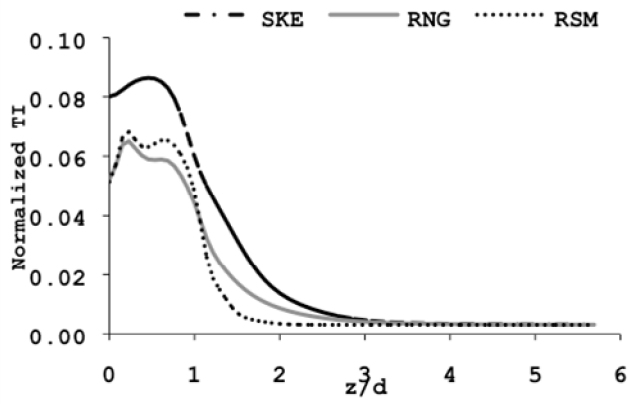


(a)

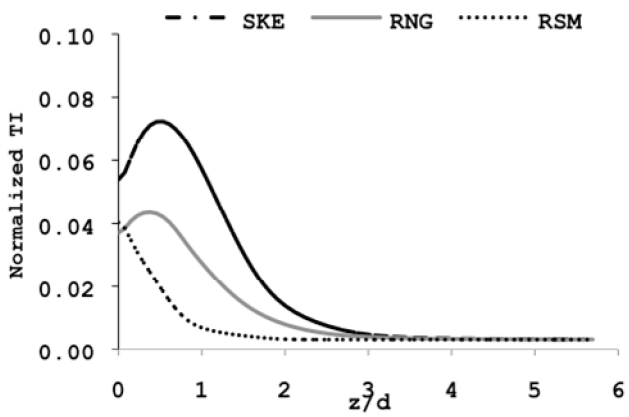


(b)

**Figure 4** Vertical profiles of predicted averaged normalized turbulence intensity for flame 1 at two downstream locations on the plane of symmetry: (a)  $x/d = 1.62$ , and (b)  $x/d = 22$ .



(a)



(b)

**Figure 5** Transverse profiles of predicted averaged normalized turbulence intensity in the wake region of flame 1: (a) wake of the jet at  $y/d = 0$ , and (b) wake of the pipe at  $y/d = -1.4$ .

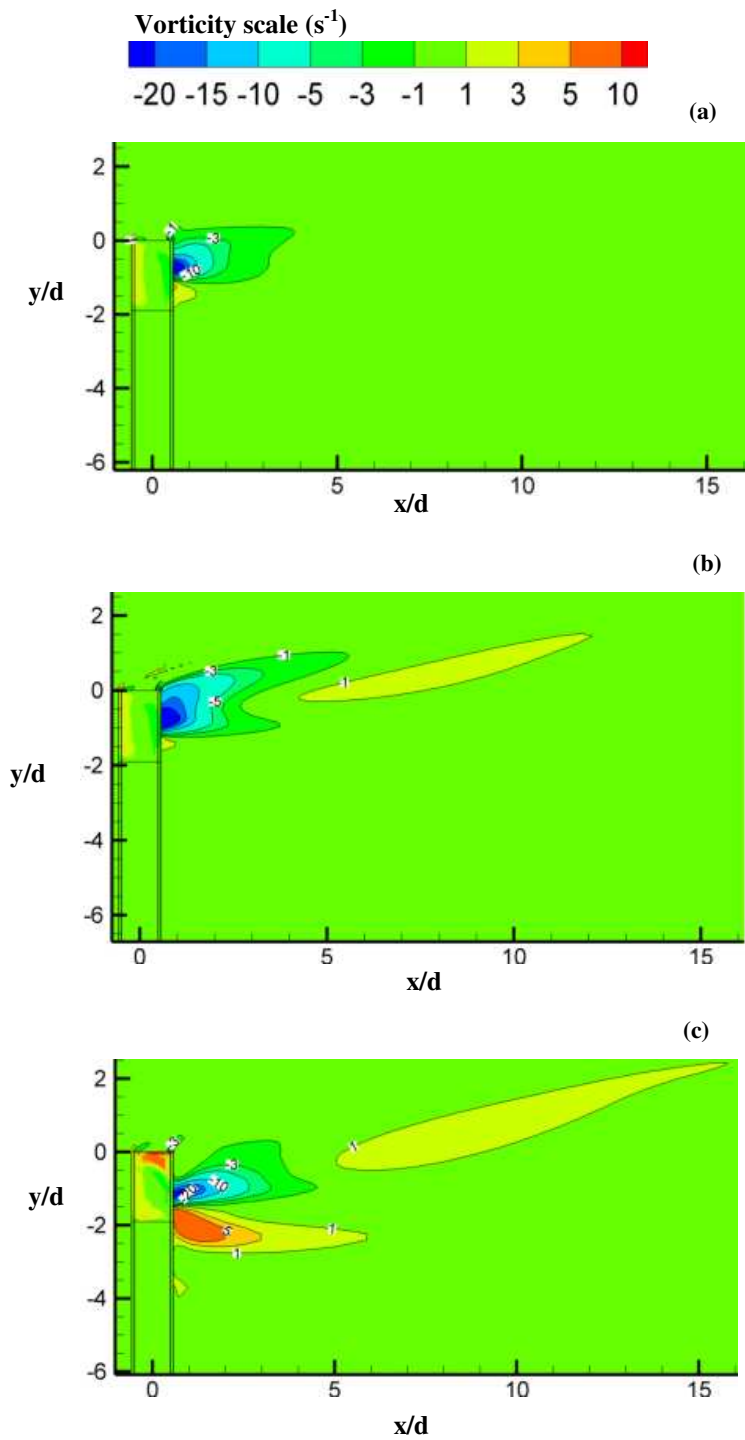


**Figure 6** Contours of the predicted normalized x-vorticity on the plane of symmetry: (a) SKE, (b) RNG, and (c) RSM models for flame 1.

Temperature scale (K)

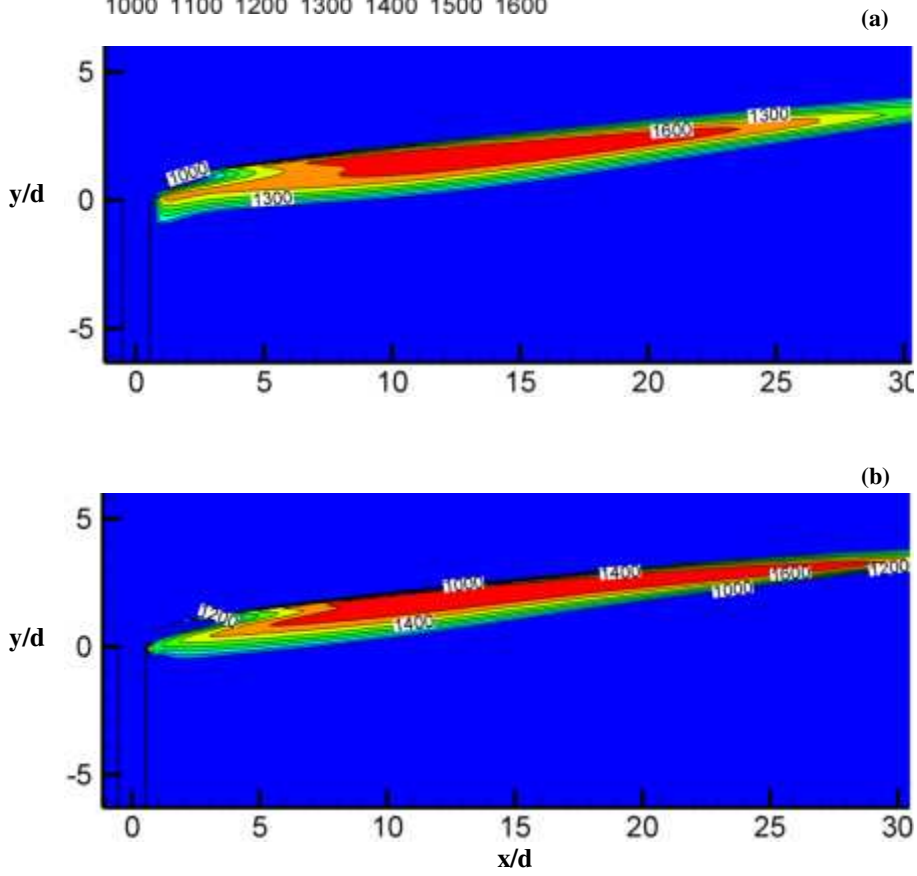
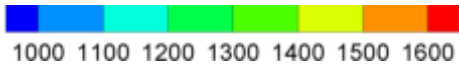
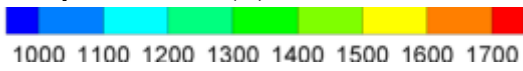
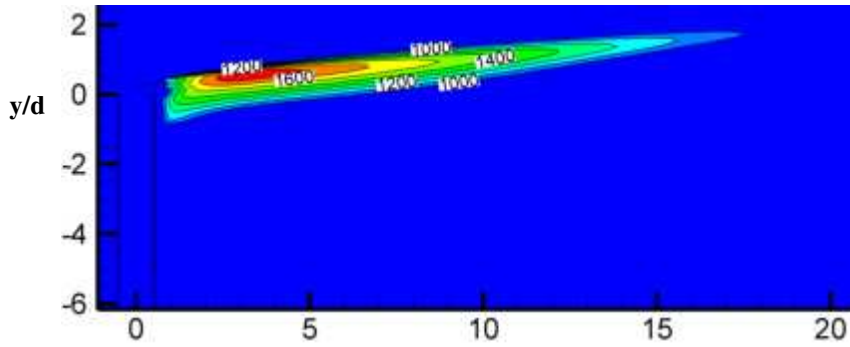


**Figure 7** Predicted temperature contours on the plane of symmetry for calculations with (a) RNG and (b) RSM. The flow conditions are for flame 6:  $u_j = 1.94 \text{ ms}^{-1}$ ,  $u_{cf} = 5.19 \text{ ms}^{-1}$ .

Temperature scale (K)



(a)



(b)

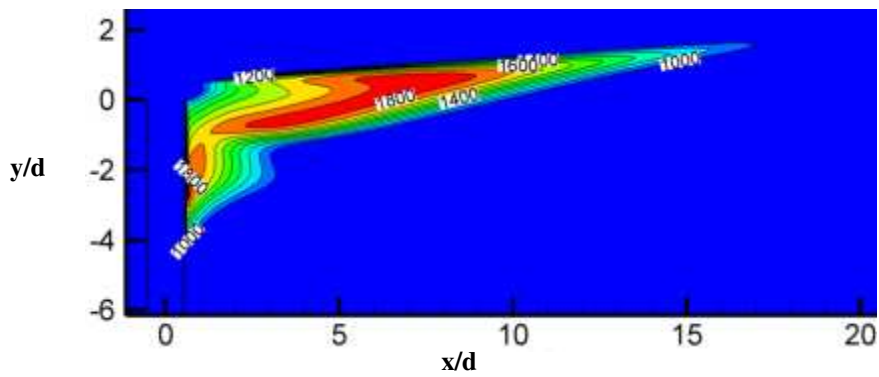
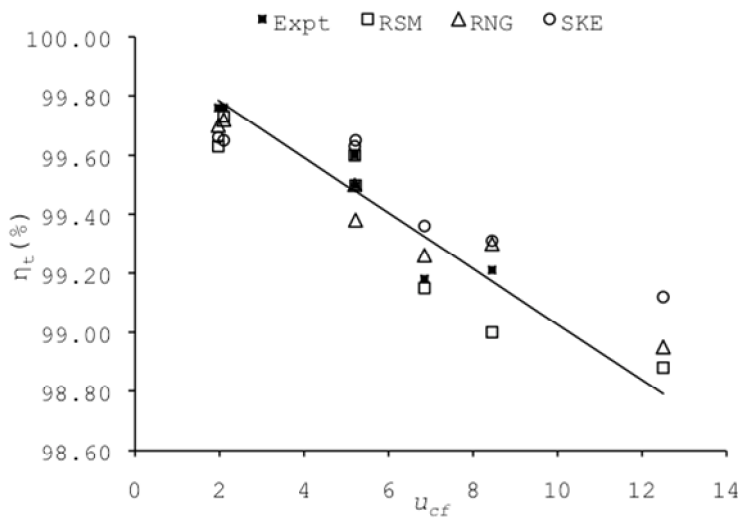
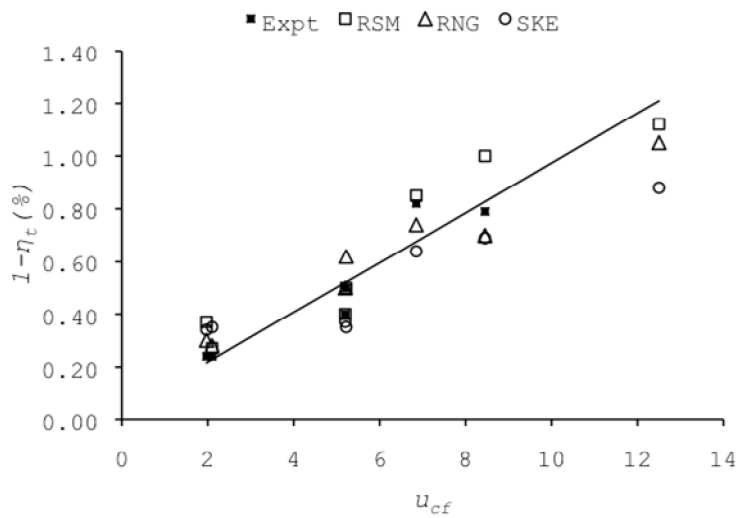


**Figure 8** Predicted temperature contours on the plane of symmetry for calculations with (a) RNG and (b) RSM. The flow conditions are for flame 7:  $u_j = 0.46 \text{ ms}^{-1}$ ,  $u_{cf} = 5.2 \text{ ms}^{-1}$ .



(a)



(b)

**Figure 9** Comparison of experimental flame combustion efficiency and inefficiency at different cross-flow velocities with predictions obtained from the three turbulence models: (a) combustion efficiency, and (b) combustion inefficiency. Straight line represent best-fit curve through the experimental data.